Journal of Dynamic Behavior of Materials (2024) 10:181–199
https://doi.org/10.1007/s40870-024-00414-0

S.I. : JDBM: DYNAMIC BEHAVIOR OF BRITTLE MATERIALS

Effect of Impact Velocity on Dynamic Crack Growth Across an Interface in Transparent Bilayers: An Experimental Study

B. M. Sundaram[1] · **H. V. Tippur**[1]

Received: 30 November 2021 / Accepted: 20 February 2024 / Published online: 22 April 2024

Abstract

The effect of impact velocity on the dynamic crack growth across a weak interface, oriented perpendicular to a mode-I crack path was studied using experiments on PMMA bilayers. This is a follow-on study of previous reports by the authors (Sundaram and Tippur in Exp Mech 56:37–57, 2016; Sundaram and Tippur in J Mech Phys Solids 96:312–332, 2016) wherein direct crack penetration or branching events were observed at a weak interface in an elastically homogeneous PMMA bilayer with different interface locations relative to the initial notch tip. The focus of this work is on the effect of impact velocity on crack growth morphology. A modified Hopkinson pressure bar was used to dynamically impact pre-cracked samples in a wedge loading configuration. Three different striker impact velocities were used and subsequent crack growth behaviors were studied with the location of the interface fixed within the bilayer. Time-resolved optical measurement of crack-tip deformations, velocity and stress intensity factor histories was performed using transmission-mode Digital Gradient Sensing (DGS) technique in conjunction with ultrahigh-speed photography. The results show that the increase in impact velocity of the striker bar promoted crack branch formation at the interface. The crack branching and penetration mechanics hypothesized by the authors in the previous report (Sundaram and Tippur in J Mech Phys Solids 96:312–332, 2016) supports this observation namely the higher stress intensity factor of the mode-I crack-tip due to increased impact velocity leads to interface debonding before the crack-tip arrival at the interface causing the crack to branch. A higher spatio-temporal resolution experiment was also carried out to obtain visual evidence to support this hypothesized mechanism. Finally, higher impact velocity promoting crack branching was evaluated for an increased interface strength and different interface location as well.

Keywords Dynamic fracture · Interfacial crack growth · Crack branching · Impact loading · Transparent armor

Introduction

Polymeric materials are attractive for transparent armor applications due to the lightweight, impact resistant and high optical transparency traits. Such structures—automotive windshields, aircraft canopies, personnel face-shields and protective enclosures, structural windows, to name a few—are often multi-layered to enhance impact energy absorption and protect personnel and/or critical instruments [1–3]. Hence, it is essential that their failure mechanics be understood for better design. Among the key factors that control the failure behavior of layered structures, the nature of crack interactions with an interface namely whether the crack gets trapped before getting deflected by the interface or directly penetrate it before propagating to the next layer is critical. The trapped crack when extends to the subsequent layer, often produces multiple deflected crack fronts consuming more energy [4] than otherwise. Many factors including interface properties, crack growth direction relative to the interface, properties of individual layers, govern crack penetration vs. deflection behavior. When the fracture toughness of the interface is lower than that of the layer, the crack tends to branch and deflect from its initial direction of propagation. An interface whose fracture toughness is comparable to the layers themselves tends to promote direct crack penetration [5–7] into the next layer. The former behavior is due to the debonding of the interface by the emanating stress waves from the growing crack tip resulting in momentary entrapment of the crack by the interface before

H.V. Tippur is a member of SEM.

✉ B. M. Sundaram
meenakshb@corning.com

[1] Department of Mechanical Engineering, Auburn University, Auburn, AL 36849, USA

branching as kinked cracks into the next layer. Furthermore, elastic and toughness mismatch between the layers and/or crack incidence angle could also affect the penetration vs. branching behavior. That is, while a crack-tip approaching an interface at a steep angle tends to penetrate the interface, the one approaching an interface at shallow angle tends to deflect into the interface [8, 9].

Several experimental techniques including caustics [10, 11], photoelasticity [8, 9, 12–14] and Coherent Gradient Sensing (CGS) [15, 16] have been used in the past to investigate dynamic interfacial crack growth in bilayers. One of the earliest studies was by Dally and Kobayashi [12] wherein the dynamic crack propagation across a similar bilayer interface, or what they called 'duplex' specimen, was studied using photelasticity. It was observed that a crack arrested at the interface for a short duration before reinitiating in the subsequent layer. Theocaris and Milios [10, 11] have studied dynamic crack propagation across bimaterial interfaces using the optical technique of caustics. They again observed that interface caused the crack to arrest momentarily before reemergence in the second material; the process of crack arrest was primarily dependent on the interface rather than the layers themselves. In certain cases where the two layers were identical, crack bifurcation was observed, which was not observed by Dally and Kobayashi. However, no correlation of these observations to the properties of the layers or the interface was reported. Riley and Dally [17], designed a model experiment wherein the wave propagation along a high impedance mismatch bilayer was investigated using dynamic photoelasticity and identified several theoretically predicted stress waves from the isochromatic fringes. The work of Tippur and Rosakis [15] examined dynamic interfacial crack growth using CGS and reported an unusually high crack velocity approaching the Rayleigh wave speed of the more compliant constituent of the bimaterial geometry as the crack propagated along the interface. Subsequent investigations reported that in such bimaterials the interface cracks could attain intersonic [8, 16, 18] and supersonic [19, 20] velocities. Xu and Rosakis [13] have visualized various failure modes involving inter-layer and intra-layer cracking in homogeneous bilayers subjected to impact loading. Further, Xu et al. [8] studied the effect of interface angle and its strength on crack penetration vs. deflection modes in homogeneous bilayers. They have reported that the angle of incidence of the crack relative to the interface plays a significant role in the mode selection. Wang and Xu [21] investigated the so-called Cook-Gordon mechanism leading to crack deflection in layered materials under dynamic loading conditions for inclined interfaces. A similar study involving inclined interfaces to study the effect of crack tip velocity on the crack deflection/penetration behavior was reported by Chalivendra and Rosakis [11]. Park and Chen [12] studied crack growth across an interface in glass bilayers using high-speed imaging and reported that the adhesive thickness affected the overall fracture behavior.

The experimental study of dynamic crack propagation in layered structures is rather challenging relative to the monolithic counterparts. Accordingly, multiple numerical investigations using finite element analyses, either using stiffness degradation techniques [22] or cohesive elements [23], and peridynamic simulations [24] have been reported on dynamic crack propagation across interfaces. Liu et al. [25] has investigated the strain rate effect on growth dynamics of a crack-tip trapped by an interface situated perpendicular to the crack path. The possibilities of interfacial crack growth as well as its emergence in the next layer as two bifurcated cracks are also examined.

In this context, authors have experimentally investigated the effect of interface namely its strength and fracture toughness relative to the layers themselves [4] and its location [26] within the bilayer on the crack penetration vs. deflection behaviors of poly(methyl methacrylate) (PMMA) when the interface was normally oriented to the approaching crack-tip. The crack velocity, stress intensity factor (SIF), and strain energy release rate histories were monitored throughout the dynamic event from the first layer into the second via the interface. It was observed that the introduction of a relatively weak interface greatly affected the crack growth behavior resulting in the occurrence of crack branch formation. However, by increasing the fracture toughness of the interface, but lower than that of the layers themselves, the interfacial crack growth could be prevented (see Fig. 1) which then can possibly transition to direct crack penetration without branching. Also, by varying the location of the interface within the bilayer geometry, the crack growth morphology can be significantly altered from direct penetration to branching behavior (see Fig. 2). Another factor that affects the crack deflection vs. penetration behavior is the projectile impact velocity, and thus the crack velocity, which is the topic of the current study.

This work examines the effect of impact velocity on crack branching behavior when a propagating mode-I crack encounters a discrete interface located normally to its path. In this experimental investigation, PMMA bilayers are dynamically loaded to initiate a mode-I crack and subsequently study its interaction with the interface at various striker velocities. The measurement of crack-tip deformations was carried out using high speed photography along with the full-field optical technique, Digital Gradient Sensing (DGS) [27], previously used by the authors to study polymers [28] and glass [29–31]. The crack tip stress intensity factors (SIFs) and crack velocities were evaluated prior to, during, and after its interaction with the interface. A mechanism for the crack path selection involving interfacial debonding is hypothesized. Furthermore, a separate experiment with higher spatial and temporal resolution to confirm

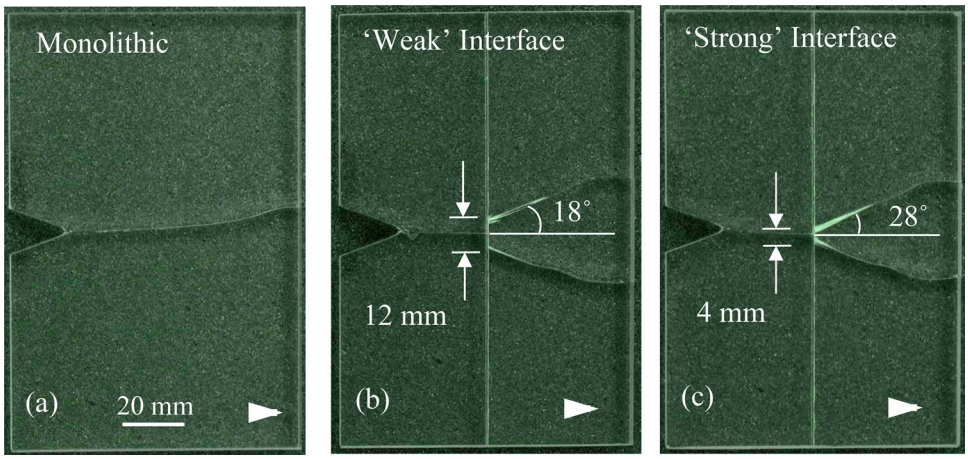

Fig. 1 Photographs of reassembled fractured specimens showing crack path selection in **a** Monolithic, **b** 'weak' bilayer, **c** 'strong' bilayer. Arrowhead indicates crack growth direction [4]

the hypothesis of interfacial debond occurrence *ahead of the propagating crack-tip* is demonstrated. In the following, a brief description of the optical method, specimen preparation/geometry, experiment setup, and the crack growth morphology for various impact velocities is presented. Next, the measured crack-tip fields and crack length histories used to evaluate velocity and SIF histories and hypothesize a crack branching mechanism are discussed. An optical setup capable of recording high temporal and spatial resolution images near the interface was used to verify the hypothesis that the emanating stress waves from the mode-I crack tip debond to the interface causing crack to branch. Empirical observations for the interplay between impact velocity and interface strength are also presented.

Optical Method

A schematic of the experiment setup used for transmission-mode DGS technique is shown in Fig. 3. In this technique [27] a random speckle pattern on a planar surface, referred to as the 'target,' is photographed through a planar, optically transparent specimen. Ordinary white light illumination is used to record random gray scales on the target. The speckle pattern is first photographed in the undeformed state of the specimen to obtain a reference image. That is, a point P on the target plane (x_0-y_0 plane) is recorded by the camera through point O on the specimen plane (x–y plane). Upon loading the specimen, the non-uniform state-of-stress alters the refractive index in the specimen including the crack-tip vicinity. The Poisson effect produces non-uniform thickness changes as well. A combination of these, called the *elasto-optic effect*, causes the light rays to deviate from their original path as they propagate in the crack-tip vicinity. The speckle pattern is once again photographed through the specimen in the deformed state. As a result, the point P appears to have shifted to point Q when recorded by the camera through point O on the specimen after deformation. The local deviations of light rays can be quantified by correlating speckle images in the deformed and reference states to obtain pseudo speckle displacements in the x- and y-directions as δ_x and δ_y, respectively. Once δ_x and δ_y are determined, the angular deflections of light rays ϕ_x and ϕ_y in two orthogonal planes namely the x–z and y–z planes, the z-axis coinciding with the optical axis of the setup and x–y being the specimen plane coordinates, can be calculated knowing the distance between the specimen and target planes. A detailed analysis shows that the local angular deflections are related to the gradients of the in-plane normal stresses as,

$$\phi_{x;y} = \pm C_\sigma B \frac{\partial(\sigma_{xx} + \sigma_{yy})}{\partial x;y}, \tag{1}$$

where C_σ is the elasto-optical constant of the specimen material, B is its initial thickness and σ_{xx} and σ_{yy} denote the thickness-wise averages.

Sample Preparation

Two cast PMMA sheets 170 mm tall and 8.6 mm thick of widths 28 mm and 72 mm were bonded along 170 × 8.6 mm faces using an acrylic adhesive to create bilayer specimens. The adhered surfaces were sanded using 400 grit sandpaper and then cleaned to remove any residue before bonding. The specimens were then machined to their final dimensions of 150 × 100 × 8.6 mm (see Fig. 4). Weldon 16, a transparent acrylic adhesive with an elastic modulus same as PMMA was used to bond the PMMA sheets to produce *elastically homogeneous* bilayer specimens with a *discrete plane of weakness*. The interface thickness was maintained as 100 µm in all the specimens by using shims during bonding. The quasi-static and dynamic crack initiation toughness values for the interface were ~ 50% and 64% that of the virgin PMMA (see "Appendix"). A 40° V-notch was machined at the mid-span of the first layer. The notch was extended

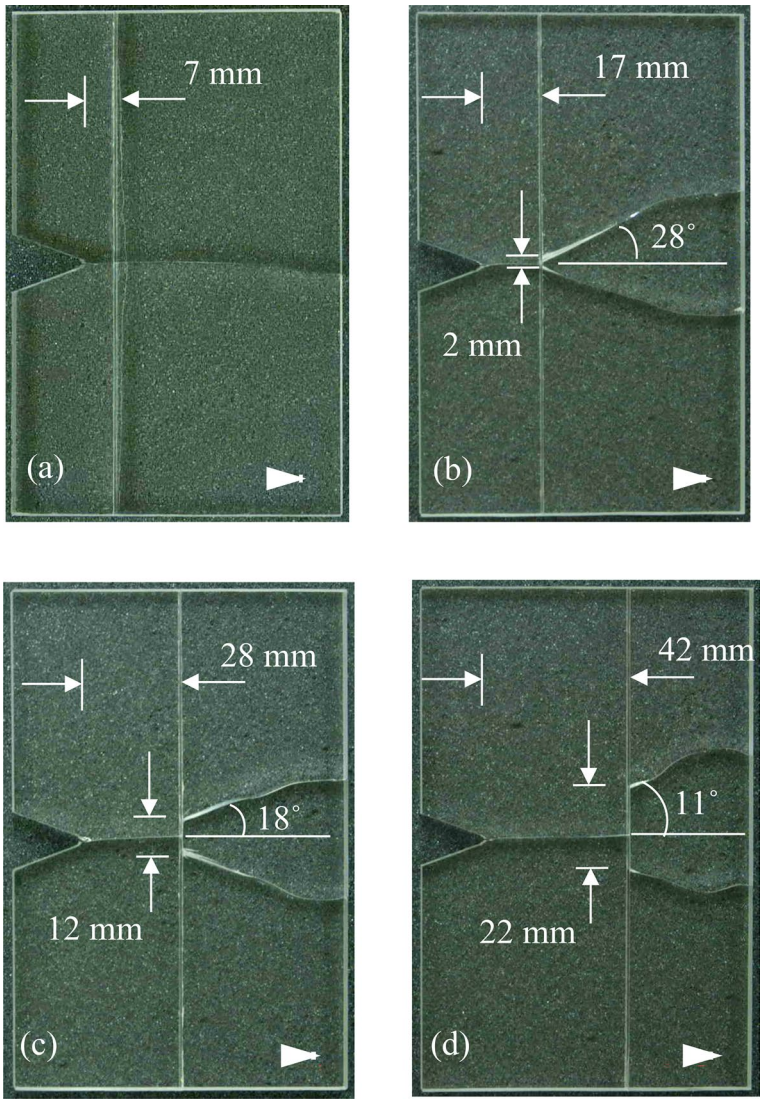

Fig. 2 Photographs of reassembled fractured specimens showing crack path selection in bilayers with 'weak' interfaces and different interface locations **a** $d = 7$ mm, **b** $d = 17$ mm, **c** $d = 28$ mm, and **d** $d = 42$ mm configurations, respectively. Arrowheads indicate crack growth direction [25]

by 2 mm using a 300 μm thick diamond impregnated circular saw resulting in a total notch length a of 21 mm. The extended notch tip was subsequently sharpened by scoring it with a steel razor blade. The dynamic properties of PMMA are listed in Table 1.

Experiment Setup

The dynamic crack growth in PMMA bilayers were studied using transmission-mode DGS in conjunction with ultrahigh-speed digital photography. The schematic of the experimental setup employed is shown in Fig. 5. A modified Hopkinson pressure bar was used for loading the pre-notched specimen. It was a 1.83 m long-bar of 25.4 mm diameter with a wedge-shaped tip pressed against an unconstrained, freestanding bilayer specimen with the matching V-notch (see, Fig. 6). A 305 mm long, 25.4 mm diameter rod held inside the barrel of a gas-gun was co-axially aligned with the Hopkinson bar and was used as the striker. Both the long-bar and the striker were made of AL 7075-T6 eliminating any impedance mismatch between them during impact.

The speckle images were acquired using a Cordin-550 ultrahigh-speed digital camera with a sensor resolution of 1000×1000 pixel and 32 independent CCD sensors positioned radially around a five-facet rotating mirror. The imaging system also included two high-energy flash lamps producing white light illumination. The experimental parameters such as the trigger delay, flash duration, framing rate, CCD gain, and data storage were controlled using a computer. A 28–300 mm focal length macro zoom lens mounted on an adjustable bellows was used for imaging the dynamic event. Further, the lens aperture was kept open as widely as possible (numerical aperture $F^{\#}5.6$) to achieve a good exposure with minimum electronic gain setting during recording. The specimen was located approximately 850 mm in front

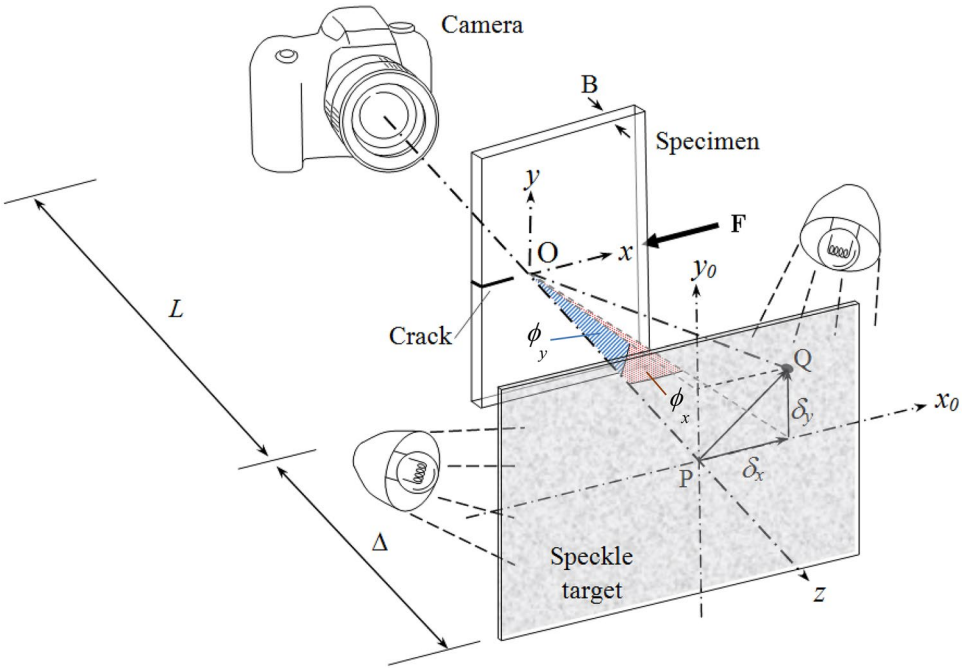

Fig. 3 The schematic of the experiment setup for transmission-mode Digital Gradient Sensing (DGS) technique to determine planar stress gradients in phase objects [27]

of the camera. (The speckle size was such that they covered 4–5 pixels on average; the scale factors were in the range of 22–24 pixels/mm.) The specimen was placed on an adjustable platform with a 2 mm thick strip of putty pressed on the top and bottom edges of the specimen, as shown in Fig. 6. The putty strips helped to achieve symmetric, approximately 'free surface' boundary conditions at the top and bottom specimen edges. A target plate covered with random black and white speckles was placed behind the specimen at a distance $\Delta = 29.3$ mm from the mid-plane of the specimen. A pair of heavy marks (see Fig. 8) on the target plate helped to relate the dimension on the image to the actual specimen/target dimensions during analysis of images.

The region-of-interest in this study was around the interface of the bilayer. Accordingly, the camera was focused on the target a square region of 45 × 45 mm on either side of the (vertical) interface. Prior to loading, a set of 32 images of the speckles were recorded in the undeformed state of the specimen at 200,000 frames per second. (The choice of the framing rate was to balance information gathering over the dynamic event covering crack growth (a) in layer-I, (b) along the interface, and then (c) in layer-II with acceptable spatial as well as temporal detail, and the capabilities of the camera.) Sufficient care was exercised to achieve an approximately Gaussian distribution of gray scales for each image by trial and error, typically in the mid-range of 0–255 (8 bit) gray scale by adjusting the flash lamp location. Next, without altering any of the camera settings, the striker was

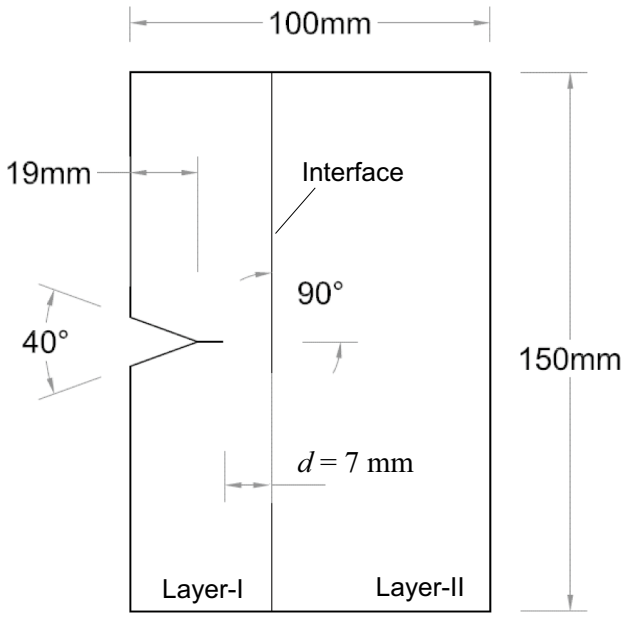

Fig. 4 Specimen configuration used for impact velocity study

Table 1 Some relevant properties of cast PMMA [4]

Parameter	Dynamic value
Density	~ 1100 kg/m^3
Elastic modulus	5.0 GPa
Poison's ratio	0.34
Elasto-optic constant	-1.08×10^{-10} m^2/N

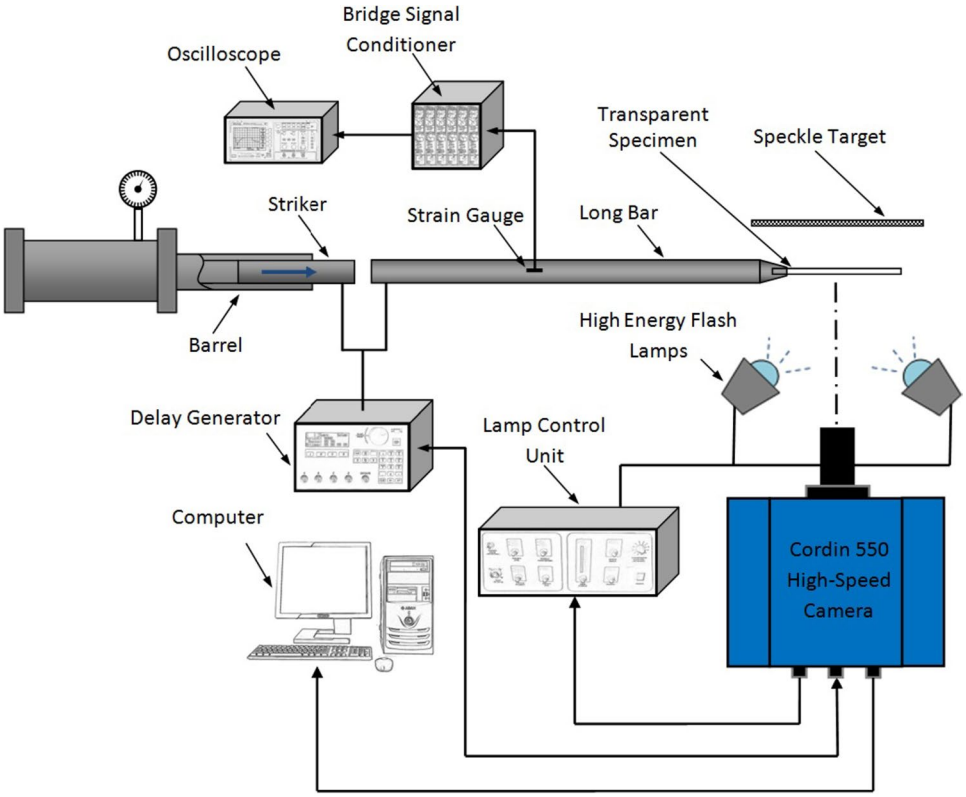

Fig. 5 Schematic of the experiment setup (top view) used

launched towards the long-bar. When the striker contacted the Hopkinson bar, a compressive stress wave was set-off in the bar, which propagated over its length before loading the specimen along the two inclined faces of the V-notch. The duration of the loading phase of the stress pulse generated was ~ 120 µs. Three different striker velocities of 13.5, 16 and 22 m/s were studied. A strain gage, placed on the long-bar recorded the incident and reflected stress pulses. The strain histories recorded on the long-bar for these three different impact velocities are shown in Fig. 7. From the figure it is evident that an increase in the impact velocity of the striker leads to higher strain amplitude and hence the transmitted energy into the specimen.

The moment the striker contacted the long-bar, a trigger signal was also produced to commence recording of a second set of 32 images corresponding to the deformed state of the specimen at the same framing rate. A trigger delay was used to account for the time taken by the stress waves to traverse the length of the long-bar before loading the specimen. Thus, a total of 32 pairs of images in the deformed and undeformed (reference) states were recorded at 5 µs intervals between successive images. Two representative speckle images in the region-of-interest, one in the undeformed (reference) state and the other in deformed state for a layered specimen configuration, are shown in Fig. 8. The speckles are noticeably distorted in the region of the propagating crack-tip (in the deformed image) whereas they seem unaffected in the far-field. The interface is evident as a gray vertical line at the center of each image. The two images corresponding to the same sensor but one in the undeformed and the other in the deformed state were paired from the two sets and each of these 32 matched pairs was correlated separately [32].

Image Processing and Data Analysis

The correlation of images was performed using the image analysis software ARAMIS®. During analysis, each image was segmented into sub-images consisting of 25×25 pixels. A sub-image overlap of 20 pixels, or a step size of 5 pixels, was also used. These chosen parameters resulted in 194×194 array of data in the region-of-interest for each of the two orthogonal displacement fields. These displacement fields were imported into MATLAB^{TM} for further analysis. The corresponding angular deflections of light rays were subsequently determined using the known distance Δ between the specimen and target planes.

The position of the crack-tip in each digitized image was used to measure the instantaneous crack length. The stress singularity at crack-tip and the resulting 'zero' contours converging towards it in the angular deflection (or stress gradient) fields, were utilized to locate the crack-tip [4]. This generally introduces errors to the computed crack

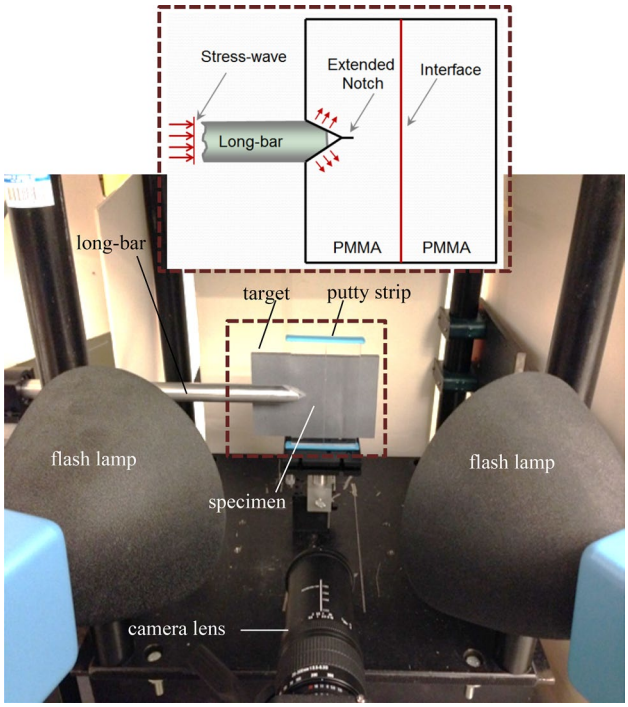

Fig. 6 Close-up photograph of the experimental setup used in dynamic fracture experiments (Inset: schematic of the loading configuration used)

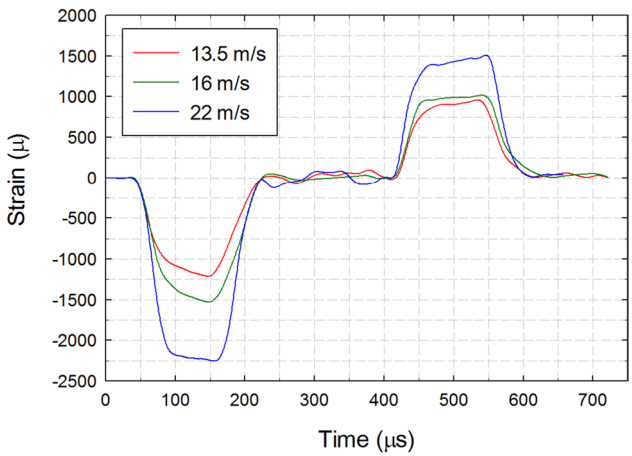

Fig. 7 Measured strain histories on the long-bar for various striker impact velocities

velocity histories obtained via numerical differentiation. To minimize such errors, a quadratic Bézier curve [33, 34] was fitted to the crack length data at a time instant 'i' as,

$$a_i(s) = (1-s)^2\hat{a}_i + 2s(1-s)\hat{a}_{i+1} + s^2\hat{a}_{i+2}, 0 \le s \le 1, \quad (2)$$

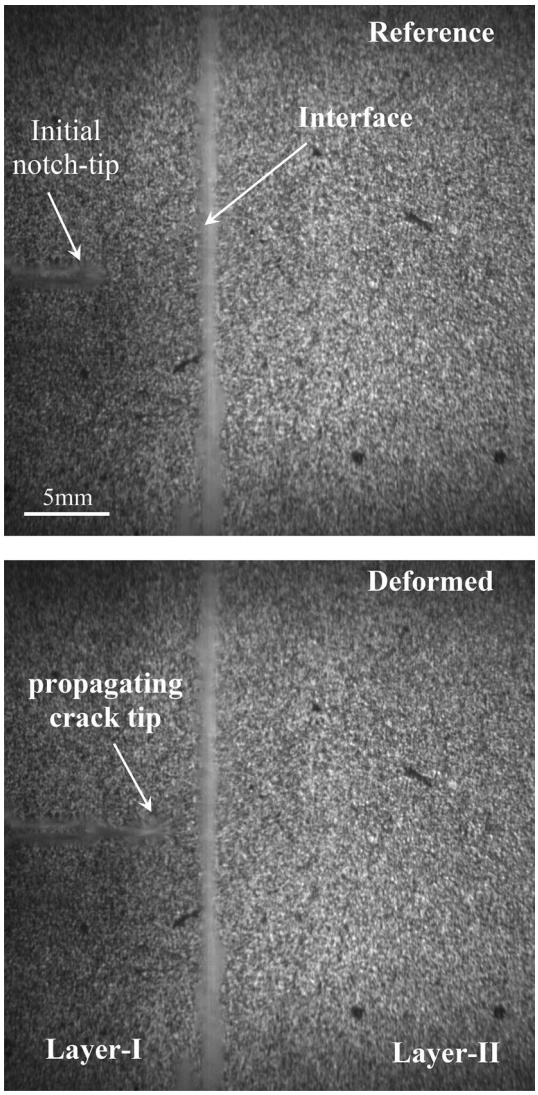

Fig. 8 Speckle images in the reference/undeformed (top) and deformed (bottom) states recorded by the high-speed camera though a PMMA bilayer

where s, $\hat{a}$ and a are the smoothing parameter, the digitized crack length, and the smoothed crack length, respectively. In the above expression $\hat{a}_i$, $\hat{a}_{i+1}$, $\hat{a}_{i+2}$ are the control points of $a_i(s)$. The value of s was 0.5 such that the smoothed data point is at the middle of the interval. The crack velocity (V) was estimated from the smoothed crack length history using backward difference method,

$$V_i = \frac{a_i - a_{i-1}}{t_i - t_{i-1}}, \quad (3)$$

where a and t are crack length and time, respectively.

Using the two orthogonal angular deflection fields, the instantaneous crack-tip fields in the local coordinates

(x', y')(x' coincides with the local crack growth direction) for a moving crack were obtained by performing coordinate transformation. The mode-I and mode-II SIFs were evaluated from an over-deterministic least-squares analysis of the crack-tip data in conjunction with the asymptotic equation (see [4] for details),

$$\begin{aligned}\phi_{x'}(t) &= \phi_x(t)\cos\theta(t) + \phi_y(t)\sin\theta(t)\\ &= C_\sigma B\left[-\frac{1}{2}r_l^{-\frac{3}{2}}\left\{f(V;C_L,C_S)A_1(t)\cos\left(\frac{3\theta_l}{2}\right)\right.\right.\\ &\quad\left.+g(V;C_L,C_S)D_1(t)\sin\left(-\frac{3\theta_l}{2}\right)\right\}\\ &\quad+\sum_{N=2}^{\infty}\left\{A_N(t)\left(\frac{N}{2}-1\right)r_l^{\left(\frac{N}{2}-2\right)}\cos\left(\left(\frac{N}{2}-2\right)\theta_l\right)\right.\\ &\quad\left.\left.+D_N(t)\left(\frac{N}{2}-1\right)r_l^{\left(\frac{N}{2}-2\right)}\sin\left(\left(\frac{N}{2}-2\right)\theta_l\right)\right\}\right],\end{aligned} \tag{4}$$

where f and g are functions of instantaneous crack velocity, and $(r_l,\ \theta_l)$ denote the contracted crack-tip polar coordinates, C_σ is the elasto-optical constant of the material, and B is its initial thickness. Further, $(r_l,\ \theta_l)$ can be expressed in the local Cartesian coordinates (x', y') as, $r_l = \left\{(x')^2 + \alpha_L^2(y')^2\right\}^{1/2}$ and $\theta_l = \tan^{-1}\left(\frac{\alpha_L y'}{x'}\right)$. The coefficients of $A_1(t)$ and $D_1(t)$ in the asymptotic series are related to the mode-I and mode-II stress intensity factors $K_I(t)$ and $K_{II}(t)$, respectively, as $A_1(t) = K_I(t)\sqrt{\frac{2}{\pi}}$ and $D_1(t) = K_{II}(t)\sqrt{\frac{2}{\pi}}$. The functions f and g in the above are,

$$f(V;C_L,C_S) = \left(\frac{1+\nu}{1-\nu}\right)\frac{\left(1+\alpha_S^2\right)\left(1-\alpha_L^2\right)}{4\alpha_L\alpha_S - \left(1+\alpha_S^2\right)^2},$$

$$g(V;C_L,C_S) = \left(\frac{1+\nu}{1-\nu}\right)\frac{2\alpha_S\left(1-\alpha_L^2\right)}{4\alpha_L\alpha_S - \left(1+\alpha_S^2\right)^2}, \tag{5}$$

where $\alpha_L = \left[1 - \frac{\rho(1-\nu)}{2\mu}V^2\right]^{\frac{1}{2}}$ and $\alpha_S = \left[1 - \frac{\rho}{\mu}V^2\right]^{\frac{1}{2}}$ for plane stress, μ and ρ are shear modulus and mass density, respectively. α_L and α_s can also be represented in terms of dilatational (C_L) and shear (C_S) wave speeds as $\alpha_L = \sqrt{\left(1 - \left(\frac{V}{C_L}\right)^2\right)}$ and $\alpha_S = \sqrt{\left(1 - \left(\frac{V}{C_S}\right)^2\right)}$ [16]. The data in the region $(0.25 < r/B < 0.75)$ and $(-135° < \theta < 135°)$ near the crack-tip was used for analysis. When mixed-mode crack growth occurred, the SIFs were used to evaluate the *effective* SIF (K_{eff}) and mode-mixity (ψ) using,

$$K_{eff}(t) = \sqrt{K_I^2(t) + K_{II}^2(t)},\ \tan\psi(t) = \frac{K_{II}(t)}{K_I(t)} \tag{6}$$

Experiment Results

Crack Path Histories

The photographs of reassembled specimens after the fracture events are shown in Fig. 9a–c. As the striker velocity V_s increased from 13.5 m/s to 16 m/s, the crack growth across the interface changed from a direct penetration into layer-II to the one that involved interface debond formation causing the mode-I crack to deflect followed by mixed-mode crack branching into layer-II. Further increase in the striker velocity did not produce significant change. That is, within the experimental variability, the crack growth at 22 m/s also resulted in crack getting trapped by the interface before branching into layer-II as mixed-mode cracks. The interface crack traveled for approx. 10 mm and 8 mm, with crack emergence angles of 26° and 21° respectively for the impact velocities of 16 m/s and 22 m/s. These experiments were quite repeatable in terms of fracture behavior and the evaluated crack-tip parameters as shown in the previous two reports by the authors [4, 26].

Crack Velocity Histories

Figure 10 shows plots of crack velocity histories for all three impact velocities used. These histories correspond to the upper branch of the branched crack configurations; the lower branches show similar history in each case [4] and are not shown for clarity. Note that $t = 0$ µs represents the time at which the crack initiated at the original notch tip. The solid-line and the dotted line circles marked on each of these three graphs represent the values at an instant before the crack enters the interface and the instant it emerges from the interface. That is, for impact velocities of 13.5, 16, and 22 m/s, the crack velocities upon the arrival at the interface were approximately 265, 355, and 351 m/s, respectively. From the plot it can be seen that the velocity histories for 16 m/s and 22 m/s striker impact follow a similar pattern whereas the lower impact velocity of 13.5 m/s has resulted in a distinctively different behavior. In the former, the crack velocity transitioned from a lower to higher value as the tip approached the interface. When it entered the interface and changed from being a single mode-I crack to bifurcated interfacial cracks, the velocity increased rapidly to a peak value. Increase in impact velocity from 16 to 22 m/s increased the peak velocities (in the interface) marginally from approximately 590 to 620 m/s. Following a rapid increase in velocity, an equally steep drop, generally close to or below the value corresponding to the one at the entrance to the interface occurred. Subsequently, these crack-tips simultaneously broke out of the interface into layer-II as mixed-mode cracks at velocities lower than when it entered

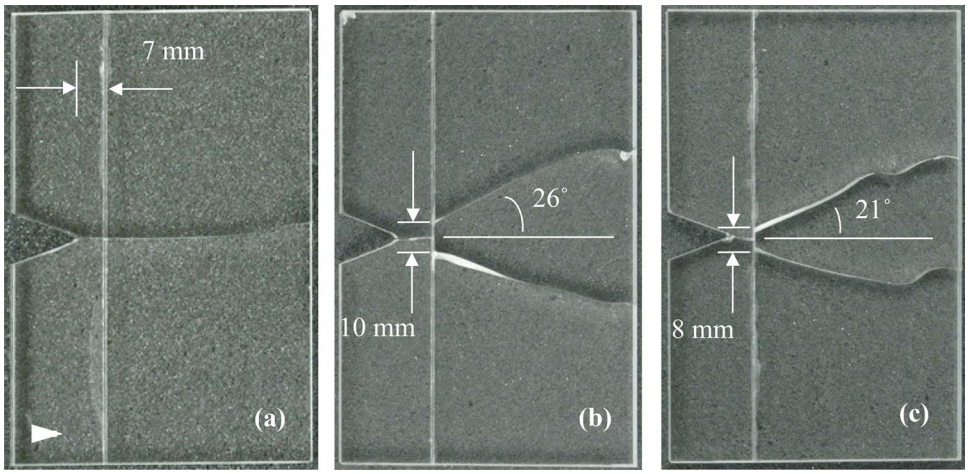

Fig. 9 Photographs of reassembled fractured specimens for different striker velocities: **a** 13.5 m/s, **b** 16 m/s, and **c** 22 m/s. Arrowhead indicates crack growth direction

the interface before increasing again. The final crack velocity was expectedly the highest for 22 m/s impact among all the cases. In contrast, for an impact velocity of 13.5 m/s, it can be observed that the velocity increased when the crack approached the interface but it continued to gain speed rather smoothly as it propagated past the interface without any interfacial growth, eventually attaining a maximum velocity of ~ 367 m/s before slowing down as it propagated further into layer-II to a final velocity of ~ 270 m/s during the observation window. The crack velocity history in layer-II for the 16 m/s is between the other two cases.

SIF Histories

The effective SIF histories (K_{eff}) and the corresponding mode-mixity (ψ) variations evaluated from DGS for all configurations are plotted in Fig. 11a and b, respectively. The effective SIF histories for the two striker impact velocities $V_s = 16$ and 22 m/s that produced crack branching show similarities whereas it is distinctly different in the unbranched ($V_s = 13.5$ m/s) case. (Again, these histories correspond to the upper branch of the bifurcated cracks and $t = 0$ represents the time at which the crack initiated at the original notch tip.) The solid-line circle marked on each of these plots represents the value at an instant before the crack enters the interface and the dotted-line circle represents the instant at which the crack emerged in layer-II from the interface. In all these cases, K_{eff} values increased monotonically as the mode-I crack approached the interface. The values of the effective SIF were significantly higher for the crack branching cases ($V_s = 16$ m/s and 22 m/s). As the interfacial debonding and bifurcated crack growth ensued along the interface, a steep drop in K_{eff} to a low value (approx. 0.6 MPa$\sqrt{\text{m}}$, below the nominal crack initiation toughness of PMMA) occurred in these two cases, resulting in a momentary arrest not detected due to the temporal resolution of 5 μs chosen to cover the entire fracture event. After the flow of additional energy into the crack tip, a gradual increase from this low value causes the interface crack to kink into layer-II at a K_{eff} lower than the one at the entrance to the interface. For $V_s = 16$ m/s and 22 m/s, when the two crack-tips exited the interface, the values of effective SIF were nearly the same. This implies that once a critical value of effective SIF was attained, the crack kinked into layer-II. As the mixed-mode crack growth in layer-II continued, an increase in K_{eff} was seen. On the contrary, in the unbranched case ($V_s = 13.5$ m/s), K_{eff} increased monotonically as the crack reached the interface, continued to increase as it penetrated the interface and then into layer-II. A gradual drop in the effective SIF ensued in this case after growing into layer-II, well-beyond the interface. The mode-mixity ψ (Fig. 11b) for the two branched cases shows similar variation whereas the one for the unbranched configuration in the entire observation window is nearly zero as expected. In the former two cases, as the crack transitioned from layer-I into the interface, a steep increase in ψ occurred due to increased mode-II SIF. The mode-mixity values when the cracks kinked into layer-II vary and for $V_s = 22$ m/s, it is marginally lower than that for 16 m/s consistent with a lower crack emergence angle in the former. During evaluation of SIFs and mode-mixites in the vicinity of the interface, enough care was taken to consider only the angular deflections corresponding to individual crack tips. Furthermore, the evaluation of fracture parameter right when all three crack tips are in proximity of the interface is prone to maximum uncertainty. However, making appropriate changes to the region of interest can minimize these effects [4].

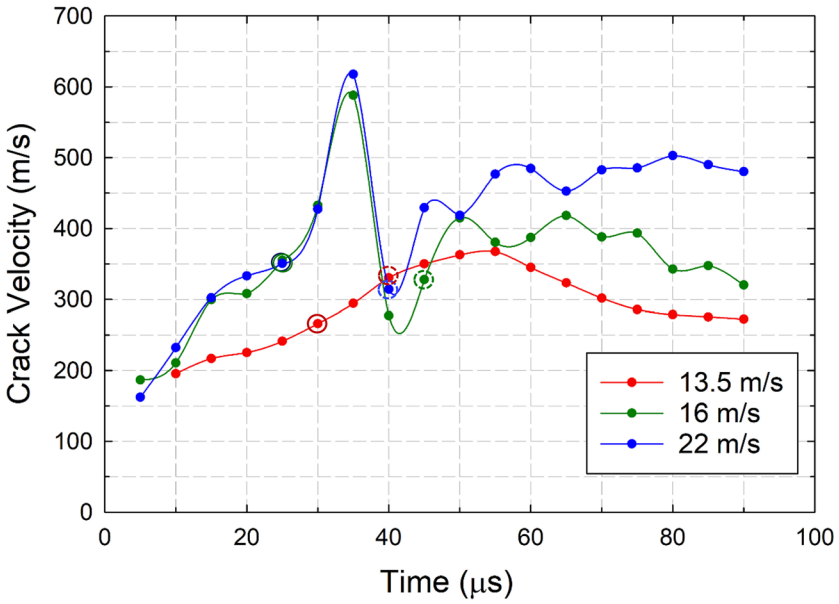

Fig. 10 Crack velocity histories for all three impact velocities for a fixed interface distance from the initial notch tip ($d = 7$ mm). The solid-line circles represent the instant before the crack enters the interface and the dotted-line circles represent the instant at which crack emerges from the interface

Discussion

Crack Penetration vs. Branching Mechanism

The observed crack penetration or deflection at an interface was examined using measured fracture parameters, namely, the instantaneous crack velocity V and SIF K_I in layer-I for each of the impact velocities. It was hypothesized that crack branching is a consequence of interface debond evolution ahead of the incoming crack tip due to the tensile stress waves *in the crack growth direction* emanating from the growing crack impinging on the weak interface [26]. The position of the crack-tip in each image prior to its arrival at the interface was used to measure the instantaneous distance r_i of the interface from the crack tip. Knowing $\theta = \theta_i = 0$ at the point-of-interest, the tensile stress on the interface in the crack growth direction was evaluated using the K-dominant expressions [35],

$$\sigma_{xx} = \frac{K_I(t<0)}{\sqrt{2\pi r_i}}\,\Sigma_{xx}(\theta=0,\,V), \tag{7}$$

where,

$$\Sigma_{xx} = \frac{1}{D}\left\{\frac{(1+\alpha_S^2)(1+2\alpha_L^2-\alpha_S^2)}{\sqrt{\gamma_L}}\cos\left(\frac{\theta_L}{2}\right) - \frac{4\alpha_S\alpha_L}{\sqrt{\gamma_S}}\cos\left(\frac{\theta_S}{2}\right)\right\}$$

$$D = 4\alpha_S\alpha_L - \left(1+\alpha_S^2\right)^2,\ \alpha_{S;L} = \sqrt{1-\left(\frac{V}{C_{S;L}}\right)^2}$$

$$\gamma_{S;L} = \sqrt{1-\left(\frac{V\sin\theta}{C_{S;L}}\right)^2},\ \tan\theta_{S;L} = \alpha_{S;L}\tan\theta$$

In the above, $K_I(t)$ is the instantaneous mode-I SIF, C_S and C_L are the shear and dilatational wave speeds, and V is the crack velocity. Figure 12a shows the histories of $(\sigma_{xx})_i$ at the interface, directly ahead of the moving crack-tip until the crack arrived at the interface. Evidently, the stress component $(\sigma_{xx})_i$ increases rapidly at the point-of-interest on the interface as the growing crack-tip approaches it. By *extrapolating the plot to* $t = 0$, $(\sigma_{xx})_i$ values as the crack-tip arrived at the interface were estimated to be approximately 20, 50, and 75 MPa for impact velocities of 13.5 m/s, 16 m/s and 22 m/s, respectively. The tensile strength of the interface was also measured independently by performing direct tension experiments on bonded specimens, as detailed in Ref. [26], and was 23 ± 0.3 MPa. The comparison between the tensile strength and the crack growth induced interfacial tensile stress for all the three impact velocities as the crack-tip approached the interface clearly shows that the 13.5 m/s impact velocity could not produce high enough tensile stress on the interface ahead of its arrival (at $t = -5$ μs) to nucleate a debond. However, 16 m/s and 22 m/s impacts drove the mode-I crack at higher velocities and higher K_{eff} to generate local tensile stresses on the interface greater than its strength (at $t = -7$ μs) nucleating an interfacial debond that led to lodging of the crack in the interface followed by branching into the next layer after some amount of interfacial growth. In other words, the interface experienced the critical tensile stress for longer duration of time in case of 16 and 22 m/s cases leading to its delamination or debonding.

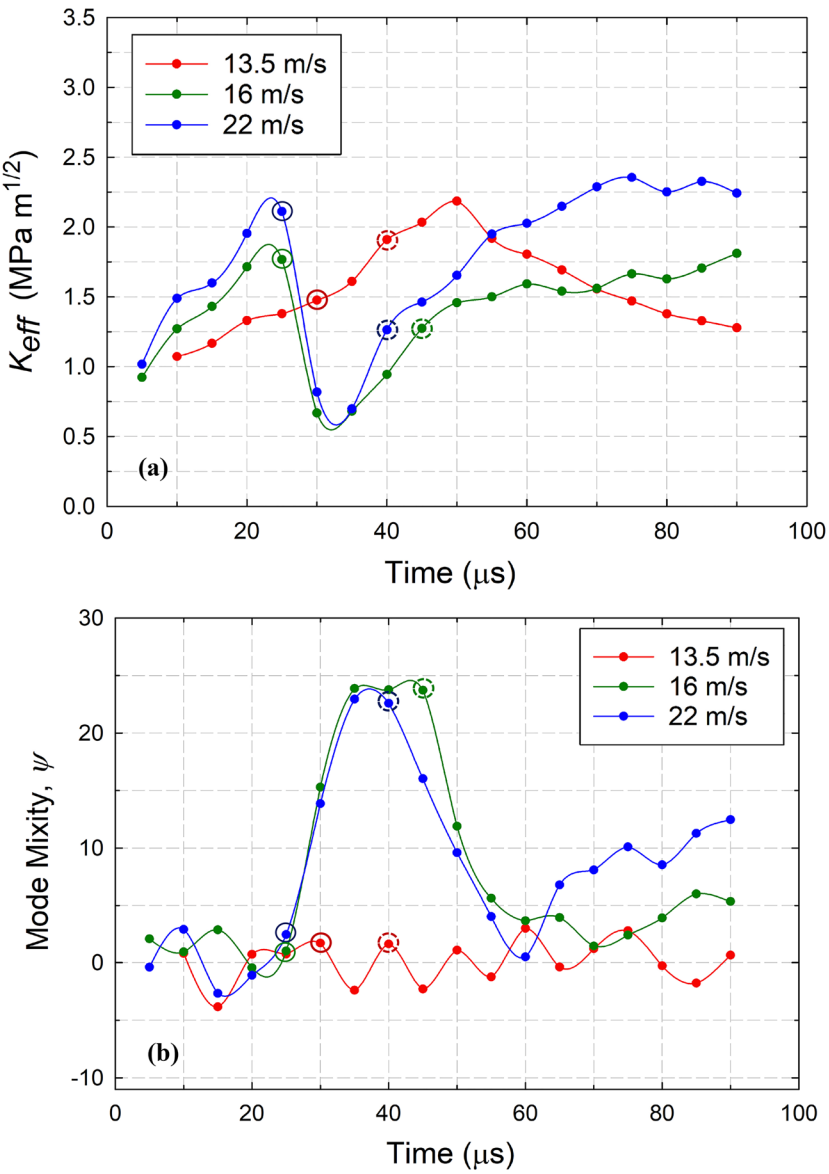

Fig. 11 History of crack-tip parameters (time $t=0$ corresponds to crack initiation at the original notch tip) for all the three impact velocities investigated: **a** effective stress intensity factor histories, and **b** mode-mixity histories. The solid-line circles represent the instant before the crack enters the interface and the dotted-line circles represent the instant at which crack emerges from the interface

In the branched crack cases, the kinking of the interface crack into layer-II was examined using the critical value of SIFs $\left(K_{eff}\right)_i \left(= \left(\sqrt{K_I^2 + K_{II}^2}\right)_i\right)$ for the 100 μm thick interface at different mode-mixities (see Fig. 12b) and mixed-mode dynamic crack initiation toughness data for PMMA (see Fig. 12c) [26, 28]. The tendency of the crack to kink out of the interface instead of continue propagating along the weak interface can be explained by the increasing critical *effective* SIF of the interface $\left(K_{eff}\right)_i$ with mode-mixity (see Fig. 12b) making it favorable for the daughter cracks to enter layer-II. Interestingly, the mode-mixity of approx. 24° and 23° were observed for impact velocity (V_s) of 16 and 22 m/s, respectively, when crack kinking occurs at the interface. The mixed-mode fracture envelope of PMMA is used to examine the favorability for crack kinking into layer-II to occur. The critical values of K_{I} and K_{II} are plotted in Fig. 12c as solid circles and the fitted band of data represents the dynamic fracture envelope for PMMA. The band captures the (a) variability of SIF during analysis of optical data, and (b) repeatability of individual experiments. The measured K_{I} and K_{II} at the instant the crack kinks or penetrates layer-II for the two higher impact velocities are plotted as green and blue solid diamond and triangle overlaid on the fracture envelope for PMMA in Fig. 12c. Also shown in this figure as a red symbol is the mode-I SIF value for the unbranched case when the crack tip had just crossed the interface. The fact that the SIF values for the emergent crack tips of branched cracks grown past the interface fall outside the fracture envelope of PMMA and the one for the unbranched case is inside the envelope adds to the explanation.

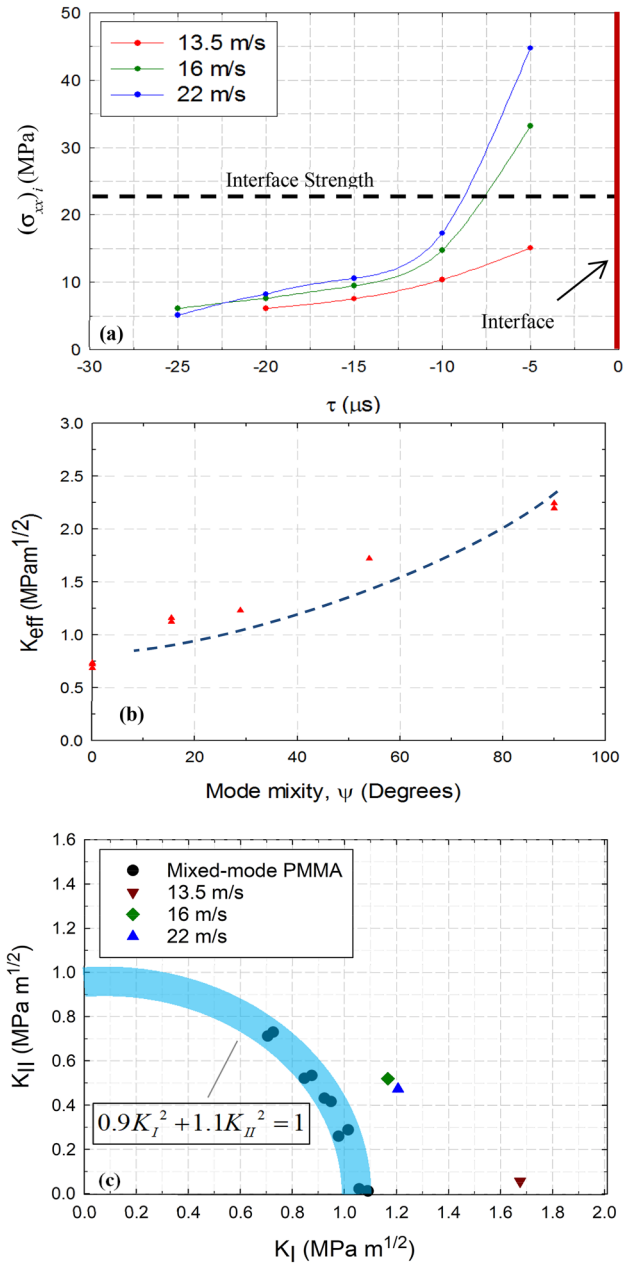

Fig. 12 Fracture characteristics of monolithic PMMA: **a** Temporal evolution of in-plane normal stress at a point on the interface directly ahead of the mode-I mother crack ($\tau = 0$ μs *corresponds to crack reaching the interface indicated by the heavy red line*), **b** Effective SIF vs. mode-mixity plot for 100 μm interface, and **c** Dynamic fracture envelope for PMMA

The marginal difference in the interface crack growth and the crack emergence angle between the two latter impact velocity cases (16 and 22 m/s) may be attributed to the increase in mode-I stress intensity factor of the crack-tip as it enters the interface. Furthermore, the decrease in the angle of emergence can also be attributed by an increase in the mode-I SIF leading to a decrease in mode-mixity during the initial phase of propagation in layer-II. Additionally, there seems to be a limit for the distance traveled by the crack along the interface. This can be ascribed to SIFs reaching a critical value favorable for the crack to kink into layer-II. When the crack neared the free surface, unstable growth occurred due to a loss of in-plane constraint.

Visualization of Interface Debond Evolution Causing Crack Branching

Next, the hypothesis that the crack branching occurs when the interface ahead of the propagating crack-tip debonds before the arrival of the mode-I crack-tip was optically tested using DGS. A specimen configuration in which the interface was situated at 42 mm from the initial notch tip [26] was used for this purpose. This configuration had previously produced crack entrapment by the interface (details in Ref. [26]) followed by a relatively significant interfacial travel prior to penetration into layer-II. The experimental details were similar to that described earlier except for was the choice of the imaging system and region-of-interest (ROI). A single sensor Kirana-05 M ultrahigh-speed camera (924 × 768 pixels) operating at five times the framing rates (1000 K fps) of Cordin-550 (200 K fps) camera (1000 × 1000 pixels) in conjunction with DGS was used for optical visualization. The camera was focused on the speckle target through the ROI on the specimen, on both sides of the interface, where a mode-I crack was expected to arrive. The ROI was approximately 30 mm × 24 mm in size. The speckle images were recorded and analyzed using ARAMIS®; here, unlike in earlier experiments with the Cordin high-speed camera, one of the speckle images well before the start of the impact loading event on the specimen was used as the reference image. Figure 13 shows a selection of recorded images along with the angular deflection contours of ϕ_y at three time instants during the nucleation of interfacial debond ahead of the growing mode-I crack tip. It can be seen from the contours that there are three discernible crack-tips in the field-of-view at each of these time instants. *It should be noted that the growing mode-I mother crack in layer-I is yet to arrive at the interface in each of these time instants.* Yet, there are two additional daughter crack-tips, evident as packed clusters of ϕ_y contours, which have bubbled up on the interface, one above and another below mother crack's prospective path. *The phenomenon can be better visualized using animations provided as supplementary material.*

Interface Strength and Interface Location with Impact Velocity

The observation that higher striker velocity promoted crack branching instead of direct penetration is somewhat counterintuitive. Yet, a Cook-Gordon-like phenomenon

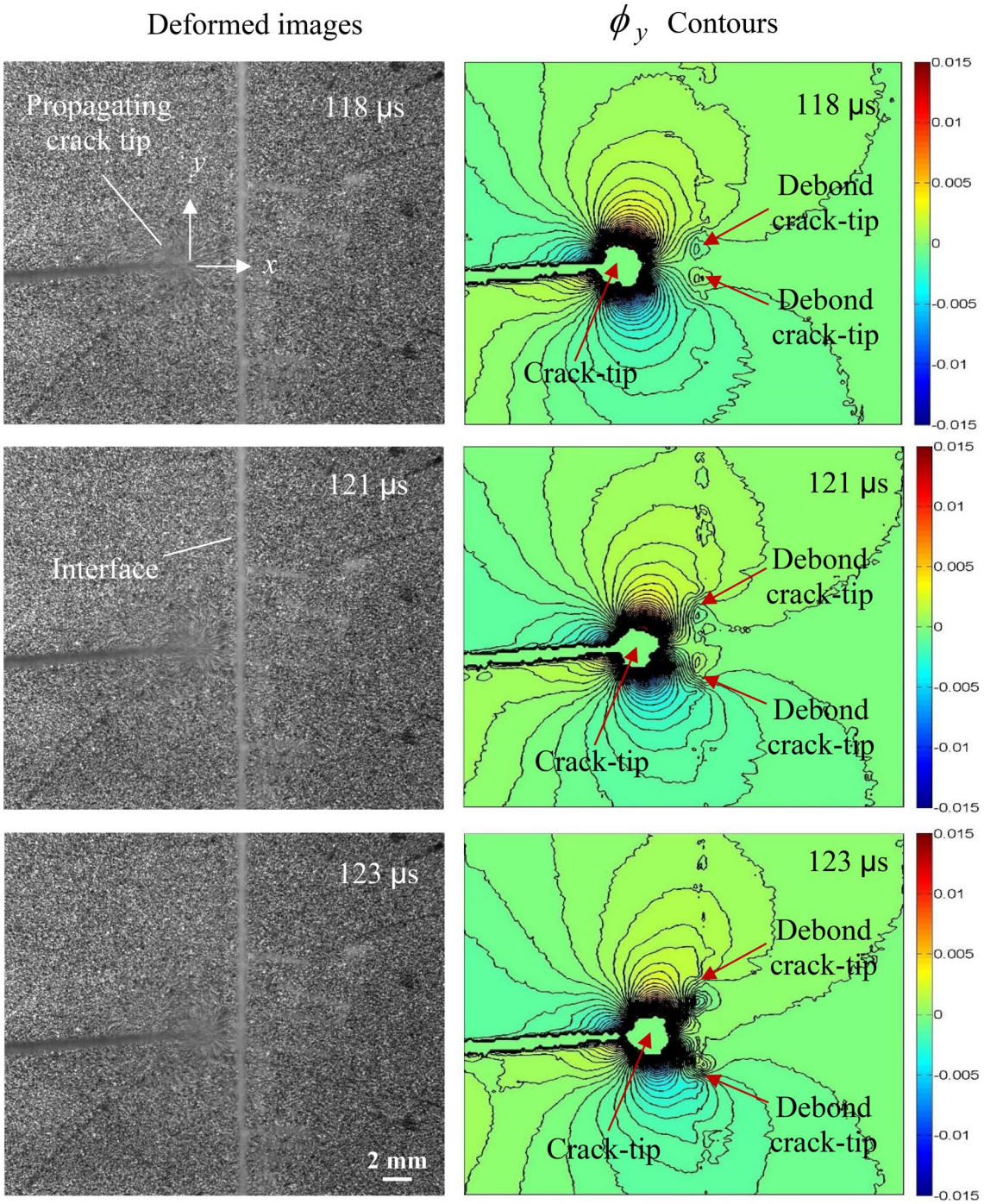

Fig. 13 The left column represents deformed images recorded at select time instants and the right column represents the corresponding angular deflection contours (contour interval = 4×10^{-4} rad) of $\varnothing_y$. The red arrows point to the location of current crack-tip and debond tips. Refer supplementary videos for more details

[36] explains reasonably well the underlying mechanics as it correlates well with the interface debond evolution ahead of a dynamically growing crack-tip. To further ascertain the conclusion that a higher impact velocity promotes crack branching is generic or limited to the current experimental setup/specimen geometry, tests were repeated for a higher interface strength (by decreasing the interface thickness; see Appendix A) and its location within the geometry. It has been reported previously by the authors that an increase in interface strength promotes crack penetration and increase in distance from the initial crack-tip promotes crack branching [4, 26]. Using the same

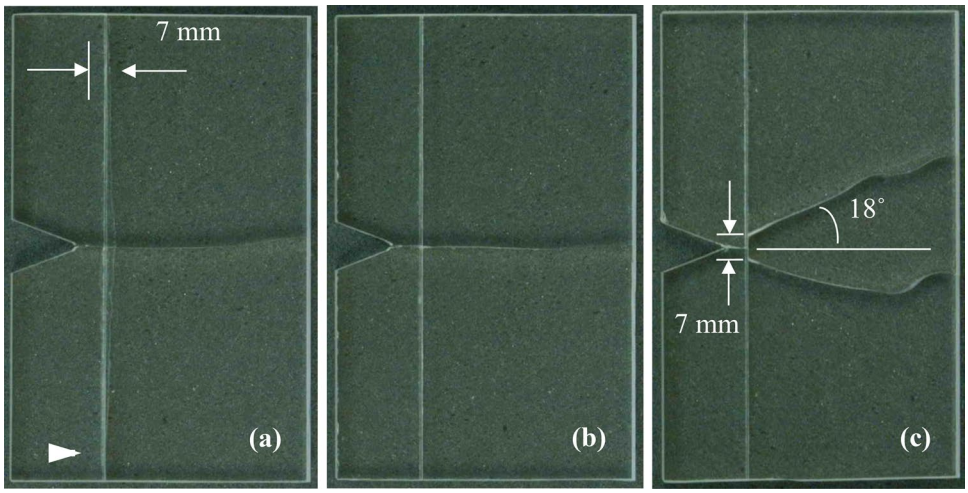

Fig. 14 Photographs of fractured specimen with $d = 7$ mm and 'strong' interface for striker impact velocity of **a** 13.5 m/s, **b** 16 m/s, and**c** 22 m/s

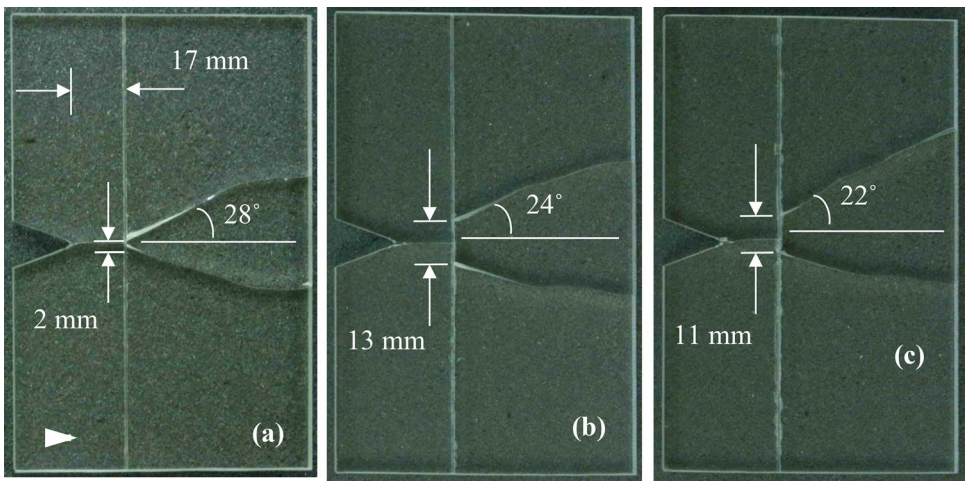

Fig. 15 Photographs of reassembled fractured specimens with $d = 17$ mm and 'weak' interface for striker impact velocities of **a** 13.5 m/s, **b** 16 m/s, and **c** 22 m/s

wedge loading configuration at different impact velocities ($V_s = 13.5$ m/s, 16 m/s, 22 m/s) a mode-I crack was driven towards the interface. The photographs of the reassembled fractured specimens are shown in Fig. 14. Since the interface was stronger in these set of specimens, the increase in the impact velocity from 13.5 m/s to 16 m/s did not produce crack branching as in the weak interface counterpart. However, with a further increase in impact velocity to 22 m/s, the crack grew faster and with a higher SIF, similar to the ones shown in Fig. 11a. This resulted in higher tensile stress σ_{xx} on the interface ahead of the growing crack which was sufficient to nucleate a debond at the interface resulting in entrapment of the incipient crack and its subsequent branching. Thus, the increase in the impact velocity caused the crack to branch. (Again, the waviness of the crack path towards the edge of the specimen can be again attributed to the loss of in-plane constraint.) This experiment was repeated for specimens with interface located farther away ($d = 17$ mm instead of 7 mm in Fig. 9) from the initial crack-tip. The photographs of the fractured specimens are shown in Fig. 15. A similar trend can be seen here. That is, with an increase in the impact velocity from 13.5 m/s to 16 m/s, an increase in the interfacial crack growth (distance crack traveled along the interface) increased from ~ 2 mm to ~ 11 mm. Further increase in the impact velocity did not produce any significant change but decreased the interfacial crack growth slightly to 11 mm. This is because the crack tip energy was significantly larger and it exceeded the fracture toughness of layer-II resulting in the emergence of cracks in the second layer more readily. Thus, increase in the striker impact velocity promoted crack branching in various specimen configurations.

Conclusions

In this study, dynamic fracture of PMMA bilayers wherein encounter between a dynamically growing mode-I crack and a normally oriented weak interface in an otherwise

homogeneous sheet were studied experimentally. This is s follow up study of earlier reports by the authors with emphasis on the effect of impact velocity on the ensuing crack penetration vs. branching mechanics at the interface. A modified Hopkinson bar in conjunction with the optical methodology of transmission-mode Digital Gradient Sensing (t-DGS) was employed in this study to record the optical distortions around the dynamically propagating crack tip that in turn translates to stress gradient fields through image processing and series of data analyses thereafter. The stress gradient fields and the position of the crack tip were used to evaluate apparent stress intensity factors and velocity histories. Apart from that, the properties of the interface such as tensile strength, shear strength, and mixed mode fracture toughness was carried out to provide a mechanics-based explanation. The major observations and conclusions of this study are:

- The mode-I crack penetrated the interface and the second layer (layer-II) of the bilayer un-perturbed when the interface at higher impact velocity resulting in higher crack-tip velocities). On the other hand, when the impact velocities were lower (hence the crack tip velocity was also relatively lower), the mode-I mother crack bifurcated into two interfacial cracks, propagated in the opposite directions by nearly equal length and then penetrated the second layer as two mixed-mode daughter cracks all the while maintaining global symmetry relative to the loading/specimen geometry.
- The distance of interfacial propagation, and the angle of emergence were affected by the magnitude of the crack tip velocity itself. Eventually however, both the daughter cracks showed a tendency to attain mode-I condition.
- Careful examination of the stress intensity factor and crack-tip velocity histories along with crack tip fields suggested that at higher incident crack velocities, the interface directly ahead of the crack-tip experienced a large enough tensile stress, exceeding the strength of the interface, nucleating a micro debond before the arrival of the incipient mode-I mother crack, resulting in two interfacial daughter cracks growing in opposite directions along the interface. The amount of interfacial crack growth increased with the incident crack velocity and continued until penetration into the second layer was energetically favorable due to a competition between mixed-mode crack growth along the interface and mixed-mode crack growth into the next layer. This is akin to the so-called Cook-Gordon mechanism under quasi-static condition.

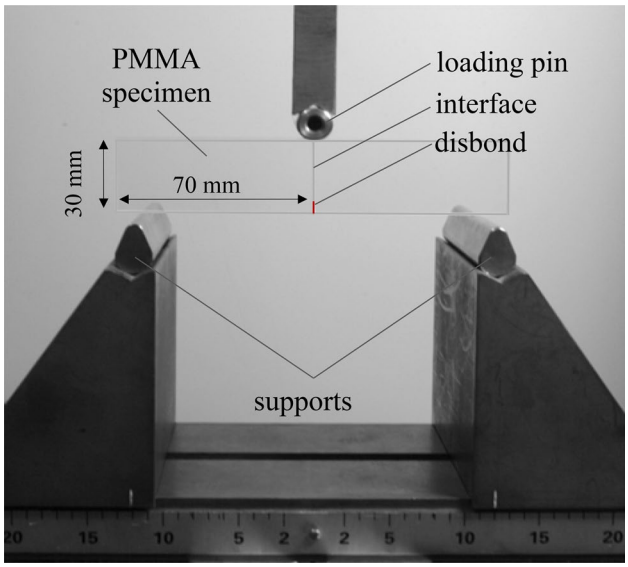

Fig. 16 Photograph of the experimental setup used to characterize interface fracture toughness

- A separate experiment was carried out with higher spatio-temporal resolution to obtain definitive evidence of the said crack-tip nucleation ahead of the incipient mode-I crack-tip. As hypothesized, the crack tip nucleated at the interface ahead of the propagating crack tip as it approached the interface.

Appendix

Quasi-static Interface Fracture Toughness

The bilayer interface was initially characterized using mode-I crack initiation toughness under quasi-static loading conditions. Symmetric 3-point bend tests on edge cracked geometries were used for this purpose. It consisted of two rectangular PMMA strips of 70 × 30 mm and thickness of 8.6 mm joined together as shown in Fig. 16. The bonded surfaces (8.6 × 30 mm) were prepared similar to the one used for making dynamic fracture specimens. The bilayer sheets with various bond layer thicknesses from 25 μm to 1.3 mm were fabricated and subsequently machined to make multiple fracture specimens from each sheet. A 3 mm long edge-disbond was introduced along the interface of each sample during preparation. The specimen was left in the vise for 24 h before performing the fracture tests.

An Instron 4465 loading machine was used to carryout symmetric 3-point bend tests. The specimen was loaded

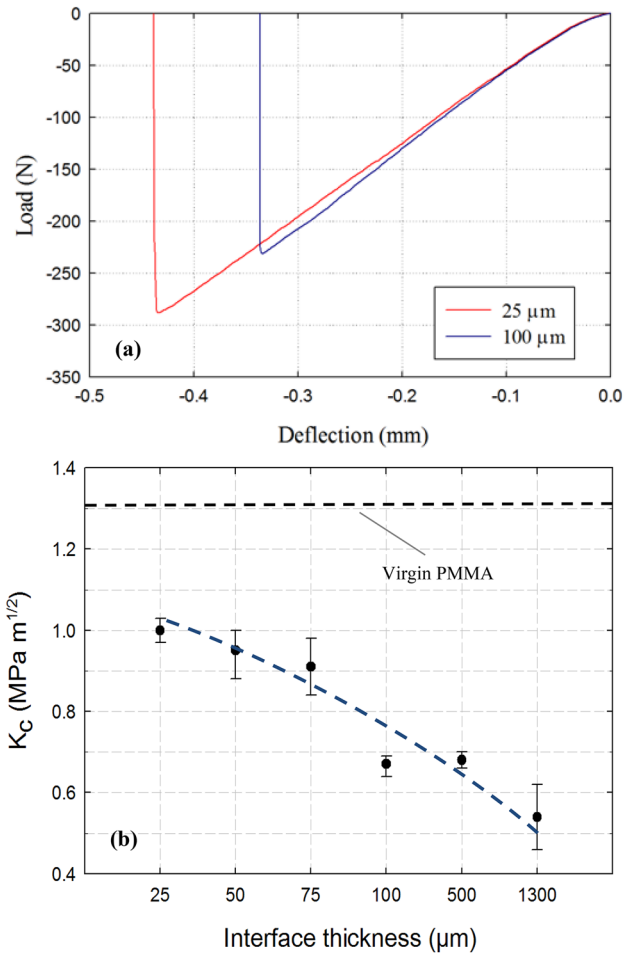

Fig. 17 **a** Measured load–deflection response for fracture specimens with 25 µm and 100 µm interface thicknesses. **b** Variation of crack initiation toughness with interface thickness. (Note that all interfaces have lower crack initiation toughness than virgin PMMA)

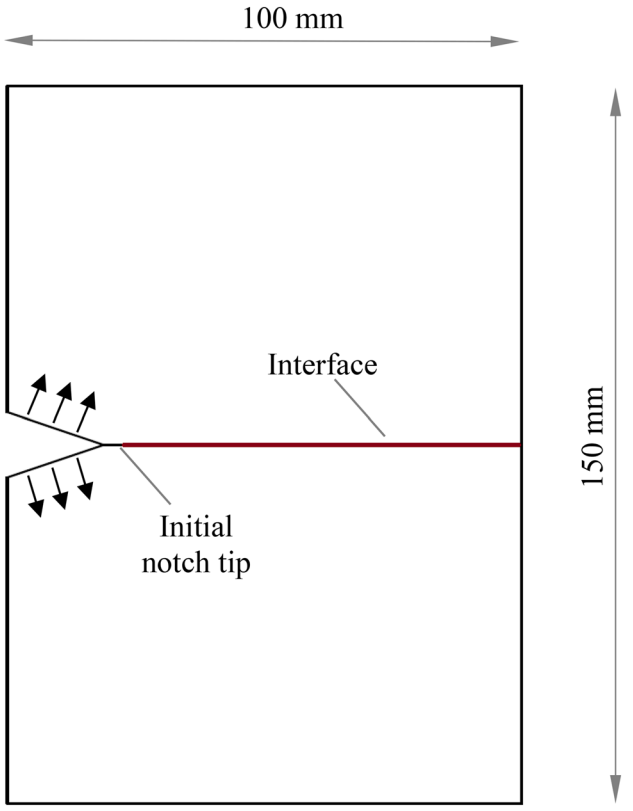

Fig. 18 Specimen geometry and loading configuration used for measuring dynamic fracture toughness of the interface by growing a crack along the interface

in displacement control mode with a crosshead speed of 0.005 mm/sec. The load was applied on the interface of the edge cracked beam samples (span = 120 mm) as shown in Fig. 16. The applied load history was recorded up to fracture. Representative load deflection plots for two select interface thicknesses are shown in Fig. 17. The samples fractured in a brittle fashion as evident from the abrupt drop in load at fracture. Using the measured peak load and the specimen geometry, the crack initiation toughness was evaluated using [4],

$$K_I = \frac{FS}{Bw^{3/2}} \frac{3(\xi)^{1/2}\left[1.99 - \xi(1-\xi)\{2.15 - 3.93(\xi) + 2.7(\xi)^2\}\right]}{2(1+2\xi)(1-\xi)^{3/2}},$$

$$\xi = \frac{a}{w}$$

The tests were repeated for various interface thicknesses to quantify the dependence of crack initiation toughness on adhesive layer thickness. The results thus obtained are plotted in Fig. 17b. It can be seen that the crack initiation toughness generally decreases with the interface thickness. Based on these results, two cases, one with an interface thickness of 25 µm and another with 100 µm were identified as 'strong' and 'weak' interfaces, respectively. The critical static mode-I SIF for neat (virgin) PMMA was also measured using symmetric 3-point bend tests and was recorded as 1.31 ± 0.07 MPa$\sqrt{\text{m}}$ (dotted line in Fig. 17b) which is *much higher than the crack initiation toughness of both interface thicknesses studied*. That is, the 'weak' and 'strong' interface crack initiation toughness were ~ 52% and ~ 77%, respectively, of that of virgin PMMA.

Dynamic Interface Fracture Toughness

The dynamic interface fracture toughness was evaluated for the interface using a Hopkinson pressure loading and DGS in conjunction with high-speed photography similar to the experimental setup discussed earlier and employed to perform full-field measurements. Two interface thicknesses of 25 µm and 100 µm ('strong' and 'weak' interfaces, respectively) were studied. The specimen geometry and loading configuration is shown in Fig. 18. The specimen preparation,

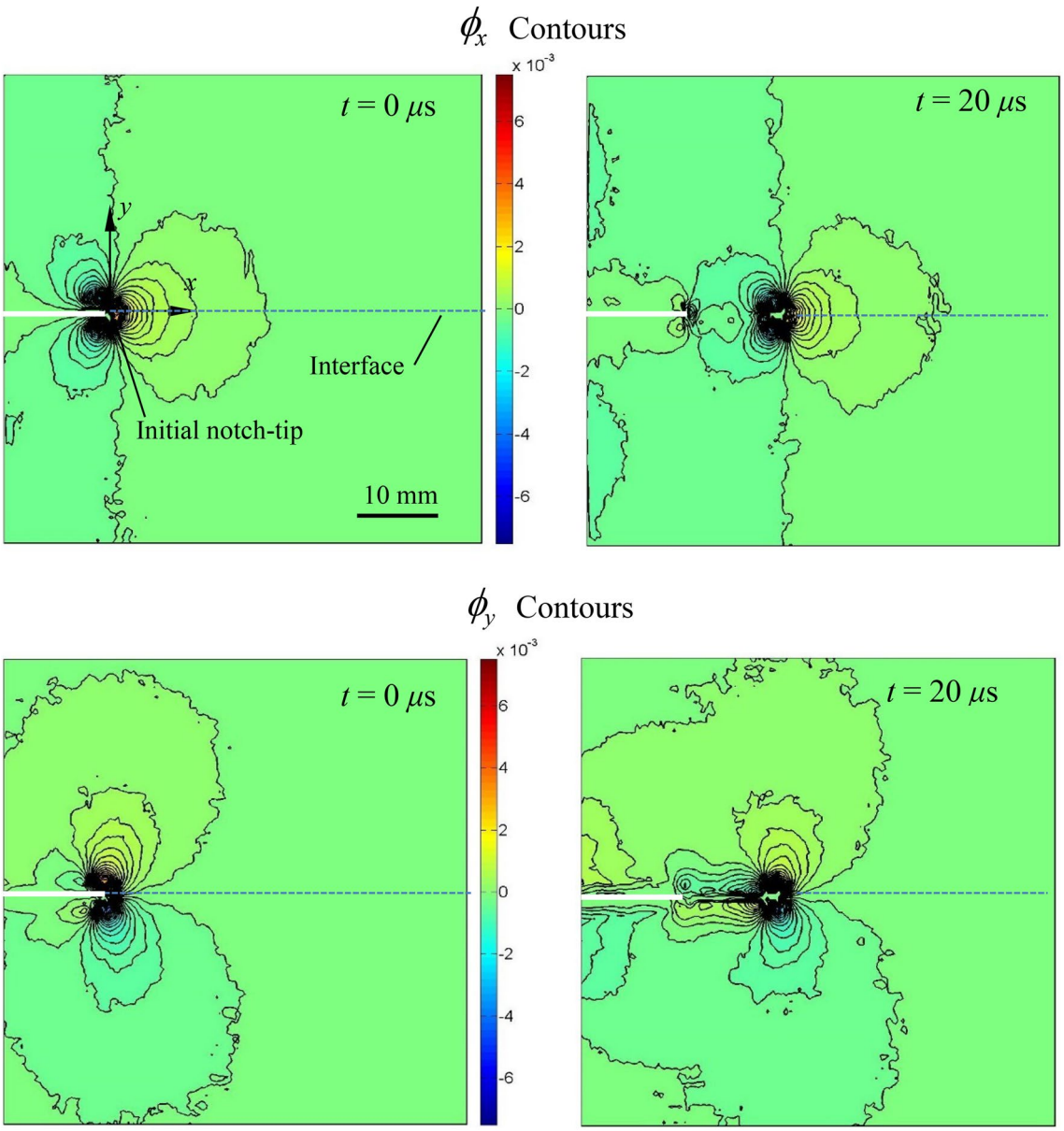

Fig. 19 Angular deflection contour plots (contour interval = 2×10^{-4} rad) proportional to stress gradients of ($\sigma_{xx} + \sigma_{yy}$) in the *x*- and *y*-directions for a 25 μm interface. ($t = 0$ corresponds to crack initiation)

experimental procedure, image analysis and evaluation of fracture parameters are identical to the ones described earlier. The in-plane orthogonal angular deflection fields at two different time instants for a 'strong' interface are shown in Fig. 19. The velocity and SIF histories for both the interface thicknesses are plotted in Fig. 20a and b, respectively. The crack speeds reached approx. 800 and 600 m/s in the 'weak' and 'strong' interface cases, respectively. These are substantially higher than the corresponding ones in a monolithic sheet, typically in the 250–300 m/s range [4]. The measured fracture toughness of the 'strong' interface (0.94 MPa$\sqrt{m}$) is higher than that of the 'weak' interface (0.72 MPa$\sqrt{m}$). When compared with the dynamic fracture toughness of PMMA (1.12 MPa$\sqrt{m}$) [28], the fracture toughness of 'weak' and 'strong' interfaces were 64% and 84%, respectively.

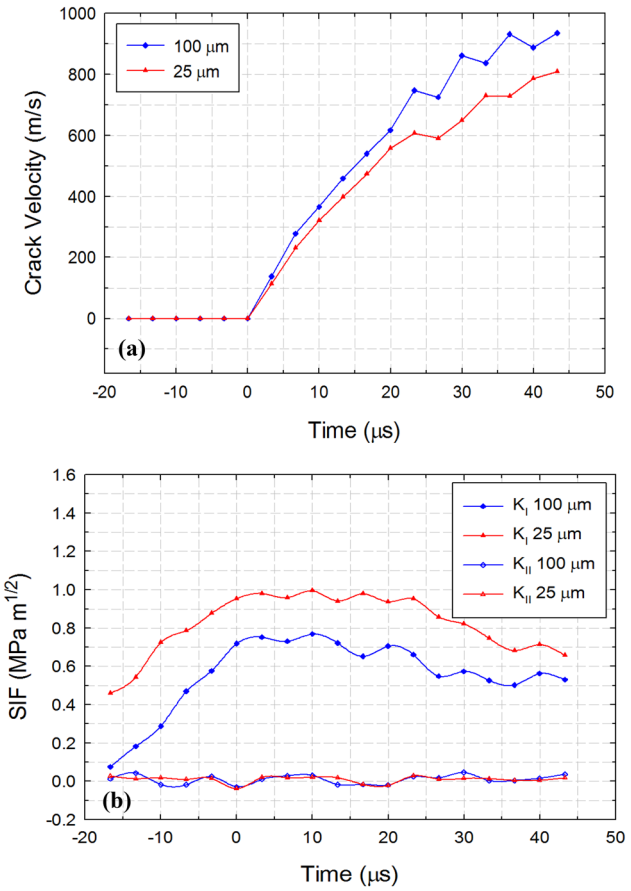

Fig. 20 Dynamic fracture parameter histories for 25 μm ('strong') and 100 μm ('weak') interfaces: **a** Crack-tip velocity histories, and **b** SIF histories

Supplementary Information The online version contains supplementary material available at https://doi.org/10.1007/s40870-024-00414-0.

Acknowledgements The support of the U.S. Army Research Office through grant W911NF-12-1-0317 is gratefully acknowledged. All authors declare that there is no other known financial or personal interest to the work reported in this paper.

Data availability Please contact the corresponding author for more information.

References

1. Freeguard GF, Marshall D (1980) Bullet-resistant glass: a review of product and process technology. Composites 11(1):25–32
2. Patel PJ, Gilde GA, Dehmer PG, McCauley JW (2000) Transparent armor. AMPTIAC Newsl 4(3):65
3. Sands JM, Patel PJ, Dehmer PG, Hseih AJ, Boyce MC (2004) Protecting the future force: transparent materials safegaurd the army's vision. AMPTIAC Quar 8(4):28–36
4. Sundaram BM, Tippur HV (2016) Dynamic crack growth normal to an interface in bi-layered materials: an experimental study using digital gradient sensing technique. Exp Mech 56:37–57
5. Suresh S, Sugimura Y, Tschegg EK (1992) Growth and fatigue crack approaching a perpendicular-oriented, bimaterial interface. Scr Metall Mater 27(9):1189–1194
6. Xu LR, Wang P (2006) Dynamic fracture mechanics of failure mode transitions along weakened interfaces in elastic solids. Eng Fract Mech 73(12):1597–1614
7. Park H, Chen W (2011) Experimental investigation on dynamic crack propagating perpendicular through interface in glass. J Appl Mech 78(5):051013
8. Xu LR, Hung YY, Rosakis AJ (2003) Dynamic crack deflection and penetration at interface in homogeneous materials: experimental studies and model predictions. J Mech Phys Solids 51(3):461–486
9. Chalivendra VB, Rosakis AJ (2008) Interaction of dynamic mode-I crack with inclined interfaces. Eng Fract Mech 75(8):2385–2397
10. Theocaris PS, Milios J (1980) Crack propagation velocities in biphase plates under static and dynamic loading. Eng Fract Mech 13(3):599–609
11. Theocaris PS, Milios J (1981) Crack-arrest at bimaterial interface. Int J Solids Struct 17(2):217–230
12. Dally JW, Kobayashi T (1978) Crack arrest in duplex specimens. Int J Solids Struct 14(2):121–129
13. Xu LR, Rosakis AJ (2003) An experimental study of impact-induced failure events in homogeneous layered materials using dynamic photoelasticity and high-speed photography. Opt Lasers Eng 40(4):263–288
14. Xu LR, Rosakis AJ (2005) Impact damage visualization of heterogeneous two-layer materials subjected to low-speed impact. Int J Damage Mech 14(3):215–233
15. Tippur HV, Rosakis AJ (1991) Quasi-static and dynamic crack growth along bimaterial interfaces: a note on crack tip field measurements using coherent gradient sensing. Exp Mech 31(3):243–251
16. Singh RP, Lambros J, Shukla A, Rosakis AJ (1997) Investigation of the mechanics of intersonic crack propagation along the bimaterial interface using coherent gradient sensing and photoelasticity. Proc Royal Soc London Ser A: Math, Phys Eng Sci 453(1967):2649–2667
17. Riley WF, Dally JW (1966) A photoelastic analysis of stress wave propagation in a layered model. Geophysics 31(5):881–899
18. Rosakis AJ, Samudrala O, Coker D (1999) Cracks faster than the sher wave speed. Science 284(5418):1337–1340
19. Winkler S, Shockey DA, Curran DR (1970) Crack propagation at supersonic velocities. Int J FractMech 6(2):151–158
20. Curran DR, Shockey DA, Winkler S (1970) Crack propagation at supersonic velocities II. Theoretial model. Int J FractMech 6(3):271–278
21. Wang P, Xu LR (2006) Dynamic interfacial debonding initiation induced by an incident crack. Int J Solids Struct 43(21):6535–6550
22. Timmel M, Kolling S, Osterrieder P, DuBois PA (2007) A finite element model for impact simulation with laminated glass. Int J Impact Eng 34(8):1465–1478
23. Siegmund T, Fleck NA, Needleman A (1997) Dynamic crack growth across interface. Int J Fract 85(4):381–402
24. Hu W, Wang Y, Yu J, Yen CF, Bobaru F (2013) Impact damage on a thin glass plate with a thin polymer backing. Int J Impact Eng 62:152–165
25. Liu LG, Ou ZC, Duan ZP, Pi AG, Huang FL (2011) Strain-rate effects on deflection/penetration of crack terminating perpendicular to bimaterial interfce under dynamic loadings. Int J Fract 167(2):135–145
26. Sundaram BM, Tippur HV (2016) Dynamics of crack penetration vs. branching at a weak interface: an experimental study. J Mech Phys Solids 96:312–332

27. Periasamy C, Tippur HV (2013) Measurement of orthogonal stress gradients due to impact load on a transparent sheet using digital gradient sensing method. Exp Mech 53(1):97–111
28. Sundaram BM, Tippur HV (2017) Dynamic mixed-mode fracture behaviours of PMMA and polycarbonate. Eng Fract Mech 176:186–212
29. Sundaram BM, Tippur HV (2018) Full-field measurement of contact-point and crack-tip deformations in soda-lime glass. Part-I: quasi-static loading. Int J Appl Glas Sci 9(1):114–122
30. Sundaram BM, Tippur HV (2018) Full-field measurement of contact-point and crack-tip deformations in soda-lime glass. Part-II: stress wave loading. Int J Appl Glas Sci 9(1):123–136
31. Sundaram BM, Tippur HV (2018) Dynamic fracture of soda-lime glass: a full-feild optical investigation of crack initiation, propagation and branching. Journal of Mechanics and Physics of Solids 120:132–153
32. Kirugulige MS, Tippur HV, Denny TS (2007) Measurement of transient deformations using digitla image correlation method and high-speed photography: application to dynamic fracture. Appl Opt 46:5083–5096
33. Prautzsch H, Boehm W, Paluszny M (2002) Bezier and B-spline techniques. Springer, Berlin
34. Jajam KC, Tippur HV (2012) Role of inclusion stiffness and interfacial strength on dynamic matrix crack growth: an experimental study. Int J Solids Struct 49(12):1127–1146
35. Freund LB (1998) Dynamic fracture mechanics. Cambridge University Press, Cambridge
36. Cook J, Gordon JE (1964) A mechnism for the control of crack propogation in all-brittle systems. Proc Royal Soc A: Math Phys Eng Sci 282(1391):508–520